Evaluation of Median Root Prior for Robust In-Beam PET Reconstruction

Us, Defne; Brzezinski, Karol; Buitenhuis, Tom; Dendooven, Peter; Ruotsalainen, Ula

Published in:
IEEE Transactions on Radiation and Plasma Medical Sciences

DOI:
10.1109/TRPMS.2018.2854231

Publication date:
2018

Evaluation of Median Root Prior for Robust In-Beam PET Reconstruction

Defne Us, *Member, IEEE*, Karol Brzezinski, Tom Buitenhuis, Peter Dendooven, *Member, IEEE*, and Ulla Ruotsalainen, *Member, IEEE*

***Abstract*—Dose delivery verification in proton beam radiotherapy is used to ensure the delivery of the dose to the correct location. A positron emission tomography (PET) scanner can be used to detect the secondary radiation during the treatment, so-called in-beam PET. This is a challenging application for PET due to the low counts and limited angular coverage. We propose a maximum *a posteriori* (MAP) reconstruction with median root prior (MRP) for the reconstruction of in-beam PET data. The proposed method was compared against MAP with total variation (TV) prior and maximum likelihood expectation maximization (MLEM), which have previously been used for this application. The effects of different ring configurations and time-of-flight information were tested with simulations of a geometrical phantom and a realistic patient treatment plan. The results indicate that both MAP methods produced sharper edges than MLEM, allowing more accurate edge localization in the reconstructed images. Even for the partial ring configurations, no elongation was observed with MAP methods. MAP-MRP successfully reduced the noise, whereas MAP-TV resulted in checkerboard artifacts. MAP-MRP was also more stable against the selection of the reconstruction parameters. In conclusion, MAP-MRP offers a simple and robust alternative for the reconstruction of in-beam PET data.**

***Index Terms*—List-mode (LM) positron emission tomography (PET), partial ring scanner, particle beam radiotherapy, proton beam radiotherapy, time-of-flight (TOF).**

I. Introduction

THE BEAMS used in particle beam radiotherapy have a well-defined, finite penetration depth with high dose deposition close to the end of the beam's trajectory, the so-called Bragg peak. This enables treatments in which less healthy tissue is irradiated as compared to irradiation with photons, leading to a reduction in irradiation-induced complications. However, as a result of the Bragg peak, large dose deposition errors can occur if the actual treatment situation is different from the situation assumed during treatment planning. An *in-vivo* technique to verify the dose delivery is thus essential to fully translate the superior dose deposition of particles into a clinical benefit.

In-vivo dose delivery verification by means of positron emission tomography (PET) created by the particle beam has a long history (see [1]–[3] for some recent reviews) and is in routine use in a few particle therapy centers [4], [5]. The most abundantly produced positron emitters are ^{15}O ($T_{1/2}$ = 2.0 min), ^{11}C ($T_{1/2}$ = 20.0 min), ^{30}P ($T_{1/2}$ = 2.5 min), and ^{38g}K ($T_{1/2}$ = 7.6 min). Unfortunately, radioactive decay process delays the information from PET, preventing real-time feedback on the dose delivery. Recent work on the production of very short-lived positron emitters may pave the way to real-time dose delivery information using PET [6], [7].

In-beam PET for *in-vivo* dose delivery verification is a challenging application for PET for two reasons. The first is the low statistics compared to conventional PET studies. At the end of a proton therapy irradiation, the PET activity is typically of the order of 1 kBq/cm^3, resulting in a small number of counts; a total of 0.04 M to 0.37 M counts were measured with a limited angle tomograph and a PET acquisition time of 200 s [8]. Such positron emitter activity and number of PET counts are much lower than those typical for diagnostic PET (10–100 kBq/cm^3 and 100–1000 M counts) and can cause the reconstructed images to very quickly converge to the noise instead of the object's true shape. Second, to allow the therapeutic beam to reach the patient unobstructed, generally scanners with limited angular coverage are used [4], [8]–[10]. A notable exception is OpenPET, in which the second generation design with slanted rings allows the beam to pass unobstructed while providing full angular coverage [11]. Partial ring scanner configurations are known to result in elongation artifacts in the direction of the detectors, hindering the accurate estimation of the edges around the irradiated volume [12]. As the accurate determination of the edges is the most important metric for *in-vivo* dose delivery verification, potential artifacts motivate an application-specific reconstruction method for in-beam PET, which reconstructs sharp edges while reducing the overall noise in the image. The use of time-of-flight (TOF) PET reduces image noise and can mitigate limited angle artifacts, but the degree of improvement by using TOF information depends on the selected reconstruction method [13].

Maximum likelihood expectation maximization (MLEM) with and without subsets has previously been used in reconstruction of PET images acquired during particle

Manuscript received January 25, 2018; revised April 21, 2018; accepted June 16, 2018. Date of publication July 10, 2018; date of current version August 31, 2018. This work was supported by the Graduate School of Tampere University of Technology and Academy of Finland under Project 305055. *(Corresponding author: Defne Us.)*

D. Us is with the Laboratory of Mathematics, Tampere University of Technology, 33720 Tampere, Finland (e-mail: defne.us@tut.fi).

K. Brzezinski, T. Buitenhuis, and P. Dendooven are with the KVI Center for Advanced Radiation Technology, University of Groningen, 9747AA Groningen, The Netherlands.

U. Ruotsalainen is with the Laboratory of Signal Processing, Tampere University of Technology, 33720 Tampere, Finland.

Color versions of one or more of the figures in this paper are available online at http://ieeexplore.ieee.org.

Digital Object Identifier 10.1109/TRPMS.2018.2854231

therapy [12], [14]–[16]. As the inversion problem is ill-posed in emission tomography, MLEM-like methods can result in the amplification of noise over the iterations, especially with low statistics data. This can be remedied by early stopping or post-smoothing, but the former can result in images that are too close to the given prior image and the latter causes blurring at the edges of the image. Maximum *a posteriori* (MAP) methods use an additional weighted penalty term in the reconstruction to prevent the amplification of noise. Any knowledge on the nature of the data, which is called a prior, can be incorporated into the MAP reconstruction. The features of the image that deviate from the prior are penalized in the reconstruction. The selected prior needs to reflect the assumptions on the data. The emission data are assumed to be locally uniform (so-called monotonicity), meaning that the pixel values of the image are approximately constant in a local neighborhood. Thus, any prior for imaging of biological structures with PET needs to allow local smoothness while preserving the edges. The total variation (TV) prior is one such prior [17]. It has earlier been suggested for particle therapy applications [13], [18], [19]. Once optimized, MAP reconstruction with TV prior (MAP-TV) outperforms MLEM. Although no artificial jumps are introduced with MAP-TV, the extremely low counts of in-beam PET data can disrupt the assumption of monotonicity and cause checkerboard artifacts [17].

In this paper, we penalize the noise using the median root prior (MRP) to accommodate the fluctuations in the data, while reducing the noise and preserving the edges [20]. MRP has previously been used for the reconstruction of Poisson-distributed data [21]–[23]. Its ability to accommodate missing detector information was demonstrated in [24]. The penalty term with MRP has not been implemented for the reconstruction of in-beam proton therapy data so far and it is proposed here because of its robustness against missing detectors and the stability of its penalty weight.

We aim to compare the performance of MAP-MRP with MLEM and MAP-TV and to determine the effects of TOF and partial ring configurations on these reconstruction methods.

II. Image Reconstruction

A. 3-D List-Mode MAP-EM

In list-mode (LM) reconstruction, events can be processed individually due to the independent nature of forward and backward projection of each line of response (LOR). This allows multiple LORs to be processed in parallel using 3-D subsets, thus speeding up the reconstruction significantly. In LM reconstruction, no preprocessing is applied, so the data statistics are preserved [25]. Without rebinning, TOF information can be fully exploited to improve the reconstruction of the LORs. In this paper, the counts were divided into L subsets ($l = 1, 2, \ldots, L$), with each subset containing h LORs. The current image estimate $x_j^{(k)}$ is updated by all L subsets and these update images are summed together to form a correction image. The system matrix calculations for each subset was distributed to multiple nodes via Techila Distributed Computing Engine[1] with MATLAB (MathWorks Inc., MA, USA). An outer-iteration consists of one pass of the current image estimate through L subsets [26]. This subset approach was proposed in [27] and also used in [26], and is referred to as LM-EM-ML due to its convergence to an ML estimate. The posterior estimate of the image with LM MAP-EM reconstruction using the one-step-late scheme can then be written as

$$x_j^{(k+1)} = \frac{x_j^{(k)}}{\sum_{i=1}^{I} A_{ij} + \beta \frac{\partial}{\partial x_j} U(x)|_{x_j = x_j^k}} \sum_{l=1}^{L} \sum_{h \in S_l} A_{i_h j} \frac{1}{\sum_{j=1}^{J} A_{i_h j} x_j^{k,l}} \tag{1}$$

where $x_j^{(k)}$ is the reconstructed value of the jth voxel in the image at the kth iteration, J is the total number of voxels to be reconstructed, and I is the total number of LORs. A_{ij} is the system response matrix, and it denotes the probability of activity in the jth voxel being detected in the ith LOR. The term $\sum_{i=1}^{I} A_{ij}$ is the sensitivity matrix. $U(x)$ is the energy function whose derivative with respect to the current image at iteration k is the penalty function. $U(x)$ determines the degree of smoothing over the voxels. The hyperparameter β determines the weight of the local regularization term. β values were chosen within the range of [0, 1] because the positivity constraint of the image values is guaranteed only if the hyperparameter value does not exceed the maximum of the normalized values in the sensitivity image. A large β increases the strength of the regularization. When $\beta = 0$, the MAP-EM becomes MLEM. The penalization is applied onto the $x_j^{(k)}$ once iterations of all L subsets within one outer iteration are completed, which prevents any instability due to the very low count statistics within each subset.

1) Median Root Prior: In MRP, the noise penalization is based on the median of the pixel values within a certain neighborhood. Its name comes from the root signal of the median filter, which passes the median filter unchanged [20]. The reconstruction algorithm with MRP assumes local monotonicity of the spatial image and it penalizes any deviation from the median in the neighborhood [28]. This enables the algorithm to preserve the edges of the image, allowing abrupt changes as well as smooth ones. The nonmonotonic features smaller than a given limit are considered as noise and are filtered out. The size of the minimum details preserved in the image depend largely on the weight of the penalization (β value) and the window size of the median filter [21]. Note that the MRP penalty term is data-driven, where the value of the median around the jth pixel, M_j, is directly calculated from the data. Therefore, the calculation of the exact derivative of the energy function $U(x)$ in (1) is not possible for MRP. Instead, the difference image between the image from the previous iteration $x_j^{(k)}$ and $M_j = \mathrm{Med}(x^{(k)}; j)$ is used. With these changes, the penalty term in (1) is calculated as $[(x_j^{(k)} - M_j)/M_j]$ [29].

2) Total Variation: The TV prior uses the norm of the image gradient as a criterion for penalization. The gradient of the image results in high values at the object boundaries, where the intensity values can be discontinuous. The TV allows these sharp changes in the image [17]. This is an important property for preservation of the edges during image reconstruction. The elongation of the object in partial ring scanners can also

[1] http://www.techilatechnologies.com/

be mitigated via TV prior [13]. The global calculation of the TV norm ensures the smoothness of monotonic regions and reduces the noise. The derivative of the energy function for TV penalty consists of partial derivatives of the image estimate. In this paper, the l1 norm was used for the calculation of the TV penalty term. The TV norm of an image A in x, y, and z dimensions is calculated by

$$\begin{aligned} &U(A)_{\mathrm{TV}} \\ &= \sum_{x,y,z} u(x,y,z) \\ &= \sum_{x,y,z} \sqrt{\left(A_{x+1,y,z} - A_{x,y,z}\right)^2 + \left(A_{x,y+1,z} - A_{x,y,z}\right)^2 + \left(A_{x,y,z+1} - A_{x,y,z}\right)^2 + \varepsilon} \end{aligned} \tag{2}$$

where e is a small parameter that prevents division by zero and ensures differentiability [17]. The penalty term in (1) is then replaced with

$$\begin{aligned} \frac{\partial U(A)}{\partial A_{x,y,z}} = &\frac{A_{x,y,z} - A_{x-1,y,z}}{u(x-1,y,z)} + \frac{A_{x,y,z} - A_{x,y-1,z}}{u(x,y-1,z)} \\ &+ \frac{A_{x,y,z} - A_{x,y,z-1}}{u(x,y,z-1)} \\ &- \frac{A_{x+1,y,z} + A_{x,y+1,z} + A_{x,y,z+1} - 3A_{x,y,z}}{u(x,y,z)}. \end{aligned} \tag{3}$$

3) Implementation: The reconstructions were performed in MATLAB 2017b with Intel X5660 processors in the Merope and Techila computing clusters of Tampere University of Technology. Monte Carlo simulations for proton therapy were conducted via Geant4 Simulation toolkit [30]. Gate (Geant4 Application in Tomographic Reconstruction, version 7.2, [31]), which is designed for nuclear medicine applications, was used for the simulation of PET system. The components of the object-related A_{ij} were calculated using Siddon's ray tracing algorithm [32]. No normalization or attenuation correction were applied before the image reconstruction in order not to change the Poisson characteristics of the data.

For the geometrical phantom, the sensitivity matrix for the scanner was computed with a separate Gate simulation, in which the field of view of the scanner was defined as vacuum with no object inside the scanner. The detector responses were recorded for a sufficiently large number of events. For the realistic phantom data, the sensitivity was computed analytically by backprojection of one count per LOR. An exact attenuation map was constructed and each LOR in A_{ij} was weighted on-the-fly with its corresponding attenuation correction factor during backprojection. Scatter and random corrections were not included in the reconstructions. Scattered events were removed from the data and randoms rate was small enough ($\sim$6% of total counts detected) for the correction to be excluded.

For the reconstruction of the geometrical phantom, 4 mm $\times$ 4 mm $\times$ 4 mm voxel size was used, resulting in image size of 81 $\times$ 81 $\times$ 45 in x, y, and z dimensions. The reconstructed image size for the realistic patient phantom was 125 $\times$ 88 $\times$ 110 voxels in x, y, and z dimensions. The window size for the median filter used in MAP-MRP was selected as [3 3 3] voxels. The reconstructed image was initialized as an array of ones for all reconstruction methods. For the reconstruction, subsets with 8000 counts were used ($h = 8000$). One hundred outer iterations were performed on the full data to investigate the convergence of the reconstructions. β values within the range of [0.01, 0.8] were tested. The hyperparameter values and the stopping criterion for the iterations were calculated for the geometrical phantom and later tested and used for the reconstruction of the realistic patient treatment plan.

The LOR endpoints were chosen to be at a depth of 8 mm in the crystal and in the center of the crystal cross section. Coincidence resolving times (CRTs) of 400 ps and 200 ps full-width-half-maximum (FWHM) were selected because 400 ps is currently available in clinical use and the 200 ps has been obtained in small-scale setups and is thus a realistic value for a future generation of scanners [13], [33], [34]. For the reconstruction with different CRTs, the exact TOF information was convolved with a Gaussian function, with an FWHM is equal to the CRT of the system. For the partial ring configurations, the detectors were removed symmetrically from either side of the scanner. The effect of angular coverage on the reconstruction methods was studied for full ring (360 degrees), 2/3 ring (240 degrees) and 1/2 ring (180 degrees) configurations, similar to the setting in [16].

III. Simulations

A. Geometrical Phantom Simulation

The geometrical phantom was used to evaluate the performance of the reconstruction methods with low count statistics and limited angular coverage. The effect of TOF information on the reconstruction was also studied. Activity densities in the range of few kBq/cm^3 were used. No proton beam was simulated for this phantom. The full-ring PET scanner configuration in the simulation contained 36 detector heads distributed in a ring of diameter 825 mm with an axial FOV of 180 mm. The 4 $\times$ 4 $\times$ 22 mm^3 LSO scintillator crystals were set in an 18 $\times$ 45 array for each detector head. The energy resolution was 13% at 511 keV, with lower and higher energy thresholds of 350 keV and 650 keV, respectively. The coincidence time window was set to 4.5 ns. Only ^{15}O production was simulated due to its high activity rate in the beginning of the proton treatment. A 60 s PET measurement with a total activity of 4.06 MBq was simulated. Fig. 1(a) shows the full and partial ring scanner configurations for the geometrical phantom.

The 12 cm-long cylindrical polyethylene nonvoxelized phantom [green circle in Fig. 1(b)] with 10 cm radius can be seen in Fig. 1(b). The hot cylinder in the phantom [red circle in Fig. 1(b)] contains radioactive water with 4 times higher activity than the background (4 kBq/cm^3 : 1 kBq/cm^3). The cold cylinder [blue circle in Fig. 1(b)] was filled with air without activity.

The list of coincidences was recorded with perfect time resolution from the simulation, containing the exact detector coordinates and the TOF information. 300 K true counts were gathered and used to construct the LM input for the reconstructions. For the 2/3 and 1/2 ring configurations, 180 K and 130 K true counts were gathered, respectively.

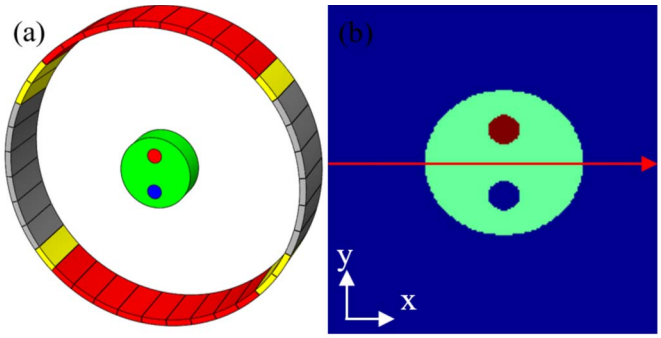

Fig. 1. (a) Scanner configurations for the PET simulation of the geometrical phantom. Gray detector heads are used in the half ring configuration (180 degrees coverage), whereas the gray + yellow blocks indicate the detector heads used for the 2/3 ring (240 degrees coverage). (b) Transverse view of the geometrical phantom. The red solid line in (b) was used to calculate the line profiles.

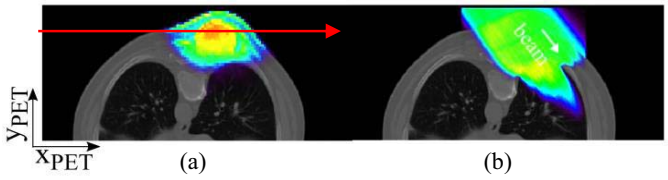

Fig. 2. (a) Realistic patient phantom with emission map overlaid on the CT image. The red arrow was used to calculate the line profiles. (b) Dose map of the third irradiation field overlaid on the CT image.

B. Realistic Phantom Simulation

For a more realistic phantom study, a proton therapy treatment plan of a patient was simulated using Geant4. The patient CT and treatment plan were obtained from the Department of Radiotherapy of the University Medical Centre in Groningen. The production of ^{10}C, ^{11}C, ^{13}N, ^{14}O, ^{15}O, ^{30}P, and ^{38}K nuclides during irradiation was simulated. The distribution and decay of these isotopes were included in the Gate simulations of the PET scans. The emission map in Fig. 2(a), representing the distribution of positron emitter decay integrated over the duration of the scan, was used as reference for the evaluation of the reconstructed images. Three proton fields were delivered to the patient, with proton beam angles of +40, 0, and −40 degrees with respect to the *y*-axis. The third irradiation field is shown in Fig. 2(b), as most of the positron annihilations detected by the scanner comes from positron emitters produced during the last field. Biological washout of the PET nuclides was implemented following the procedure of Helmbrecht *et al.* [35], using one washout component with a half-life of 69 s and a fraction of 0.44. A 120 s scan was simulated with 60 s delay after the delivery of the last field. The PET scanner used in this simulation was based on the Siemens Biograph64 PET/CT with TrueV option (Siemens Molecular Imaging, Knoxville, USA). The energy resolution was set to 13% at 511 keV, with lower and higher energy thresholds of 350 keV and 650 keV, respectively. The coincidence time window was set to 4.5 ns. The attenuation map was obtained from the bilinear scaling of the HU values in the CT scan of the patient [36]. The total activity was 5.9 MBq (1 kBq/cm^3) 60 s after the delivery of the last field. The dose delivered at the target area was about 2 Gy in total (similar to the dose delivered in [18]), a typical value for a daily fraction of the irradiation treatment. The full ring scanner simulation included 4.28 M true counts. The 2/3 and 1/2 ring configurations resulted in 3.25 M and 2.35 M true counts, respectively.

C. Assessment Criteria

The normalized mutual information (NMI) measures the similarity of information between two images, giving the value of 1 if two images are identical [13]. It was used to select the optimal weight of the penalization (β) for TV and MRP as well as the stopping criteria for the MAP methods [13]. The standard deviation across 2-D slices was also calculated as a measure of uncertainty. The NMI is calculated through the Shannon entropy of the images. The Shannon entropy of an image (H) is defined as

$$H = -\sum_i p(i)\log p(i) \tag{4}$$

where the probability $p(i)$ that the value of the ith voxel occurs is calculated from the histogram of the image. Let the respective entropies of two images A and B be $H(A)$ and $H(B)$. $H(A, B)$ represents the entropy of the joint histogram of two images. The mutual information between A and B, MI(A, B), is then

$$\mathrm{MI}(A, B) = H(A) + H(B) - H(A, B). \tag{5}$$

Using MI(A, B), the NMI is calculated as follows:

$$\mathrm{NMI}(A, B) = \frac{\mathrm{MI}(A, B)}{\sqrt{H(A)H(B)}}. \tag{6}$$

Bias between the reconstructed images and the ground truth was used to evaluate the reconstruction accuracy. The bias between the reconstructed image A and the reference image B is calculated as

$$\mathrm{Bias} = \frac{\mathrm{mean}(A) - \mathrm{mean}(B)}{\mathrm{mean}(B)} \times 100. \tag{7}$$

The coefficient of variation (CoV) was used to evaluate the level of noise reduction in the reconstructed images. Each CoV was calculated within a volume of interest (VOI) using

$$\mathrm{CoV} = \frac{\sigma_{\mathrm{VOI}}}{\mu_{\mathrm{VOI}}} \tag{8}$$

where σ_{VOI} is the standard deviation of the voxels within a VOI, and μ_{VOI} is the mean value of these voxels. A low CoV indicates low noise in the image, whereas a high CoV is a sign of high noise within the VOI.

Sigmoid functions were fitted to the edges of the reconstructed images to calculate and compare their accuracy in determining the edges. The following sigmoid function sig(h) was used in this paper:

$$\mathrm{sig}(h) = \mathrm{base} + \frac{\max}{1 + \exp\left(\frac{h_0 - h}{b}\right)} \tag{9}$$

where h is the pixel index along the line profile. The "base" is set to zero as there is no activity outside of the phantom. h_0 is

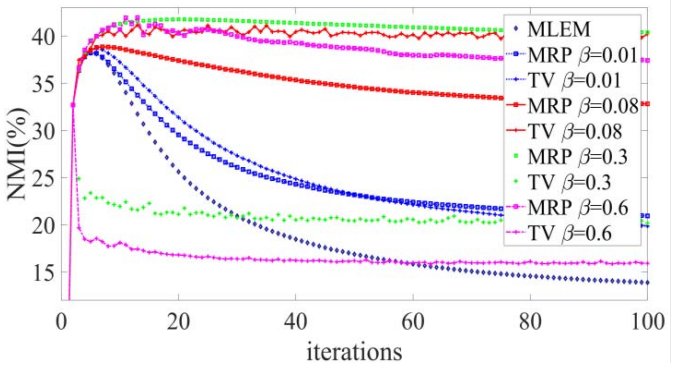

Fig. 3. NMI (%) values for selected β values over 100 iterations. NMI values were calculated over the 3-D image volume from the 2/3 ring scanner with 400 ps CRT.

the position at which 50% of the (max-base) value is reached. b is a measure for the steepness of the edge. A smaller b shows a steeper edge and a more accurate determination of the distal edge.

Iso-contour comparison was used for the evaluation of the realistic phantom reconstructions. As the iso-contours are used for dose calculations in clinical practice, they were preferred over the reconstructed images for visual comparison of the realistic phantom images.

IV. Results

A. Results of the Geometrical Phantom

Before the comparison of reconstruction methods, the optimal penalization weight and number of iterations for the MAP reconstructions were determined. In MAP reconstruction, β determines the strength of penalization. The hyperparameter that maximizes the 3-D NMI and stabilizes over iterations was selected as optimal for each prior. Fig. 3 shows the NMI values for several β over 100 iterations for 2/3 ring scanner with 400 ps CRT. The trend of the NMI values obtained from reconstructions with other partial ring configurations and CRT values show a similar pattern.

It can be seen from Fig. 3 that a stable maximum NMI is achieved at $\beta = 0.3$ for MRP and $\beta = 0.08$ for TV. For TV, the NMI values rapidly decrease when β is greater than 0.08. The MRP results become stable at $\beta = 0.3$ and, for higher values, image blurring as well as the distortion of the first and last slices in the axial (z) dimension, due to 3-D filtering, cause the NMI to decrease over iterations. In the selection of number of iterations, the dominant concern was the stability of the reconstructions, therefore a high number of iterations were selected for MAP methods. It was observed that the NMI values of MAP reconstructions for the selected β values stabilize after 50 iterations (Fig. 3). All MAP reconstructions evaluated from hereon were thus obtained after 50 iterations. As NMI values of MLEM decrease over iterations, seven iterations were used.

Fig. 4 shows the reconstructed images from the geometrical phantom for both CRT values and all scanner configurations. The summed slices are shown here similar to [37]. The effect of the missing detectors in the partial ring scanners is clearly visible for images reconstructed via MLEM with 400 ps CRT, resulting in the elongation along the direction of the detectors. These effects are reduced by the improved TOF information. Both MAP reconstructions have clear boundaries and less elongation. As the overall reconstruction is already better for MAP methods than MLEM, the effect of improved TOF is less pronounced on MAP than MLEM reconstructions.

TABLE I
Bias, Cov, and Sigmoid Fit Parameters for the Geometrical Phantom (True h_0 Is at Pixel 65.53, $b = 0$)

	Full ring 400ps	Full ring 200ps	2/3 ring 400ps	2/3 ring 200ps	1/2 ring 400ps	1/2 ring 200ps
Bias (%)						
MLEM	-52.5 ± 1.2	-50 ± 1.2	-42.9 ± 1.4	-43.9 ± 1.8	-41.2 ± 5.5	-45.5 ± 3.8
MAP-MRP	-28.6 ± 1.6	-29.6 ± 1.4	-31.2 ± 0.8	-32.2 ± 1.1	-31.6 ± 3.3	-34 ± 3.1
MAP-TV	-28.3 ± 2.1	-31.1 ± 1.8	-32 ± 2.3	-33.2 ± 2	-33.2 ± 7.7	-35.6 ± 5.3
CoV (%)						
MLEM	63.3 ± 7.5	66 ± 7.3	60 ± 5.8	65.7 ± 6.1	64.9 ± 5.9	70 ± 6.5
MAP-MRP	38.6 ± 1.2	38.6 ± 1.2	45.5 ± 1.04	43.8 ± 1.03	52.9 ± 1.9	50.2 ± 1.7
MAP-TV	42.6 ± 6.4	40.6 ± 5.5	46.9 ± 6.5	44.5 ± 5	52.3 ± 5.6	50.5 ± 3.8
h₀						
MLEM	65.5 ± 0.44	65.5 ± 0.46	63.1 ± 0.78	63.4 ± 0.75	63.4 ± 0.75	63.5 ± 0.52
MAP-MRP	65.1 ± 0.16	65.2 ± 0.14	63.2 ± 0.41	64 ± 0.32	62.5 ± 0.41	63.6 ± 0.35
MAP-TV	65.3 ± 0.13	66 ±0.10	63.2 ± 0.33	64 ± 0.38	63 ± 0.32	64 ± 0.30
b						
MLEM	-0.6 ± 0.37	-0.4 ± 0.36	-2 ± 0.66	-1.2 ± 0.65	-2 ± 0.63	-0.6 ± 0.45
MAP-MRP	-0.3 ± 0.29	-0.3 ± 0.17	-0.9 ± 0.36	-0.9 ± 0.28	-0.5 ± 0.34	-0.4 ± 0.26
MAP-TV	-0.4 ± 0.1	-0.1 ± 0.01	-1.2 ± 0.29	-1.1 ± 0.33	-0.6 ± 0.28	-0.6 ± 0.27

Table I gives the mean of bias and CoV as well as the sigmoid fit parameters for the reconstructions. The uncertainty reported here is the standard deviation across different slices. Bias and CoV values were calculated through the uniform volume in the background cylinder, excluding the areas near the hot and cold volumes to avoid spilling of activity from the high activity regions in case of elongation.

The MAP-MRP reconstructions achieved the best bias and CoV for most of the studied cases, as well as smallest standard deviation across slices. The MAP-TV performs slightly worse than the MAP-MRP for partial rings, but its CoV and bias are still significantly lower than those of MLEM. Better TOF slightly improves the contrast recovery and the fitting of the sigmoid function of MAP methods, particularly in partial ring configurations. Both bias and CoV indicates worse performance for MLEM for 200 ps compared to 400 ps.

The accuracy of the reconstructed edges was evaluated by fitting sigmoid functions to the line profiles (see Table I). The sigmoid fit was calculated from the average of the central slice and its two closest neighbors in the axial direction. As the

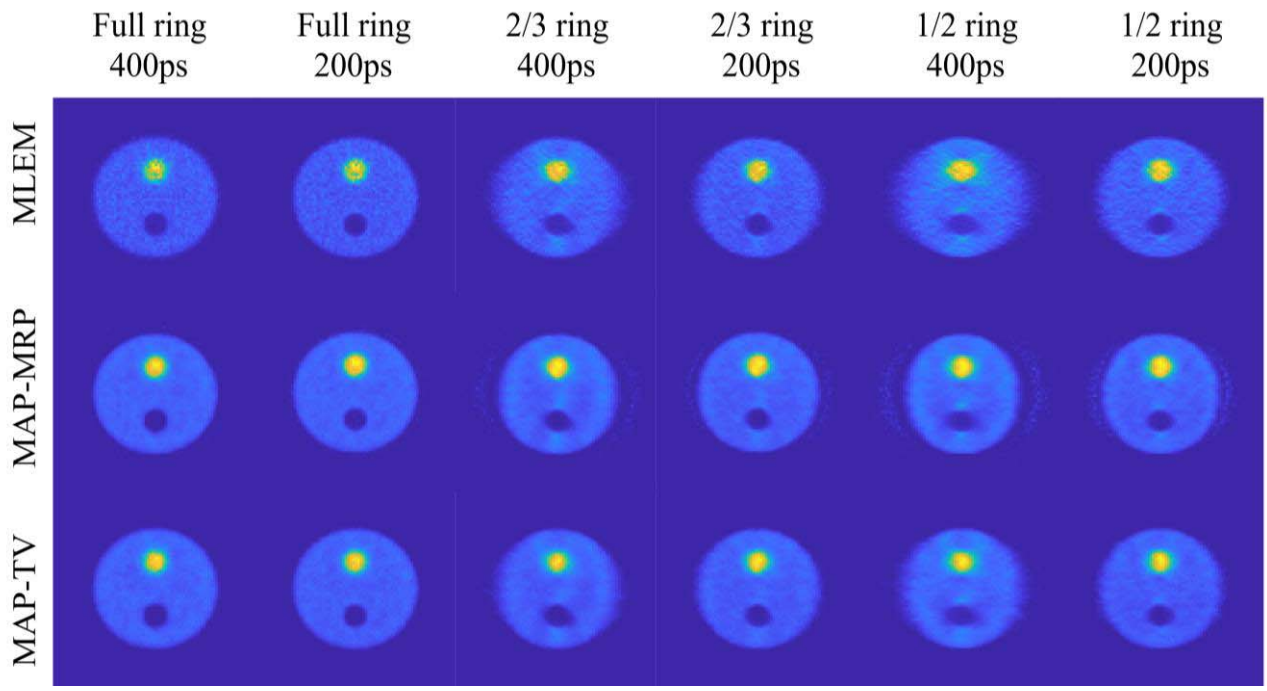

Fig. 4. Reconstructed images from sum of transverse slices. The intensities in each image are normalized within the range of [0,1] after the extreme values are excluded from the image. Rows 1, 2, and 3 depict the MLEM, MAP-MRP, and MAP-TV reconstructions, respectively. MLEM images were stopped after seven iterations. The MRP and TV prior reconstructions are presented here with their optimal β values after 50 iterations ($\beta = 0.3$ for MRP and $\beta = 0.08$ for TV). The elongation along the x direction is visible for the partial ring reconstructions for MAP-TV and MLEM.

falling edge was used in the calculation of the fit, the slope (b) is negative. When comparing the accuracy of the sigmoid fits, the edge of the ground truth was taken as reference, with h_0 at 65.53 and $b = 0$.

All sigmoid fits for the full ring configuration indicate high accuracy of results, though the uncertainties on the fit parameters are smaller for MAP. For the partial ring configurations, the MAP methods demonstrated a sharper edge than MLEM for both CRT values. All partial ring reconstructions showed improvement with 200 ps CRT.

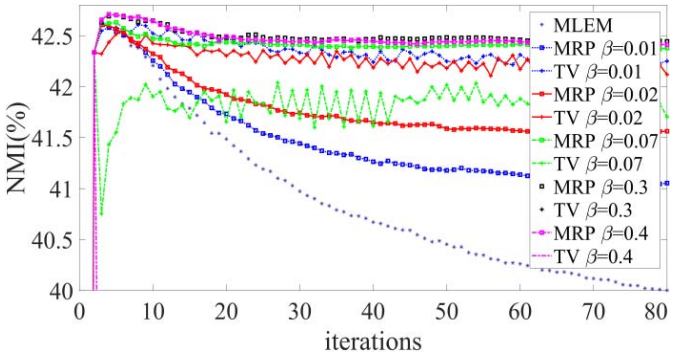

Fig. 5. NMI values for the studied β values for the realistic phantom from the 2/3 ring scanner with 400 ps CRT. NMI values were calculated over the whole image volume.

B. Results of the Realistic Patient Phantom

Before the evaluation of the reconstructed images, the reconstruction parameters were tested for the realistic patient phantom. According to the NMI values for various β in Fig. 5, optimal β was selected as 0.02 for TV. β was 0.3 for MRP.

In proton therapy, the iso-contours are commonly used to evaluate the treatment plan. In this paper, they were used as indications of the relative intensities for each reconstructed image to make the differences between the images more visible. The iso-contours of the emission map overlaid on the CT image and the reconstructed images can be seen in Fig. 6. The iso-contours from the MAP reconstructions follow the shape of the contours in the emission activity well, with MRP resulting in better reconstructions of the irregular contours (see the white arrow in Fig. 6. Also, the contours of the high intensity regions (80% of the maximum activity marked in red in Fig. 6) in MAP-MRP reconstructions are visually more similar to the emission map than MLEM and MAP-TV. The MAP-TV reconstructions have poorer performance with low statistics data and they do not recover uniform high intensity areas. This is visible from the red iso-contour areas in Fig. 6 (marking 80% of the maximum activity, respectively).

Table II shows the bias and CoV values as well as the sigmoid fit parameters for the reconstructions of the realistic phantom. The bias values were calculated using the normalized reconstructions and emission map. Iso-contour lines were used to create a homogenous VOI for the calculation of the bias and CoV values of the realistic phantom. The red iso-contour line at the center of the emission image (80% of the maximum value within the slice) was used as a threshold to obtain an approximately homogenous volume. The CoV value for the same volume in the emission image was 5.16%.

The bias and CoV of the partial ring reconstructions were the best for MAP-MRP. The improvement of CRT did not

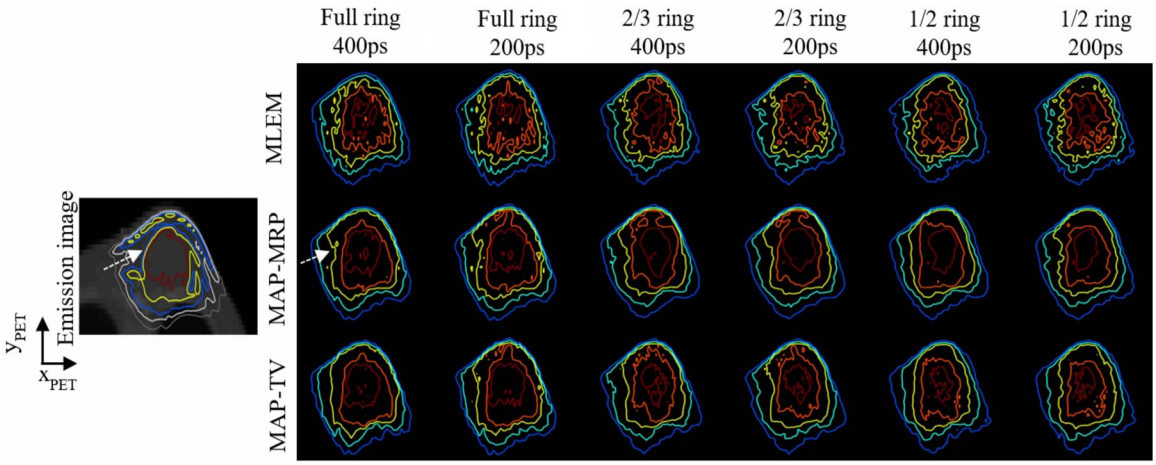

Fig. 6. Transverse view of the reconstructions from the realistic phantom with iso-contours. Fifty iterations were used for MAP-MRP and MAP-TV reconstructions ($\beta = 0.3$ for MRP and $\beta = 0.02$ for TV). MLEM reconstructions were stopped after seven iterations.

TABLE II
BIAS, COV VALUES, AND SIGMOID FIT PARAMETERS FOR THE REALISTIC PHANTOM (TRUE h_0 IS AT PIXEL 53.41, $b = 0$)

	Full ring 400ps	**Full ring 200ps**	**2/3 ring 400ps**	**2/3 ring 200ps**	**1/2 ring 400ps**	**1/2 ring 200ps**
Bias (%)						
MLEM	-16.5 ± 5.3	-17.6 ± 4.8	-19.5 ± 6.9	-21.5 ± 6.9	-22 ± 6.3	-22.1 ± 7.1
MAP-MRP	-6.7 ± 2.6	-6.9 ± 2.7	-8.3 ± 4.8	-9.3 ± 4.5	-10.2 ± 5.7	-9.9 ± 4.8
MAP-TV	-8.64 ± 4.5	8.03 ± 4.02	-14.63 ± 5.3	-14.13 ± 4.4	-15.81 ± 5.7	-14.94 ± 4.4
CoV (%)						
MLEM	12.4 ± 1.9	12.7 ± 1.8	14.9 ± 3.2	15.2 ± 3	15.9 ± 3.2	16.2 ± 3.3
MAP-MRP	9 ± 1.3	8.8 ± 1.3	11.1 ± 3.4	10.97 ± 3	11.7 ± 3	11.4 ± 2.8
MAP-TV	9.22 ± 1.9	9 ± 1.6	13.2 ± 2.9	12.5 ± 2.5	13.2 ± 3.1	12.5 ± 2.9
h_0						
MLEM	54.18 ± 0.09	53.86 ± 0.06	54.24 ± 0.09	53.76 ± 0.06	54.82 ± 0.18	54.08 ± 0.09
MAP-MRP	53.25 ± 0.04	53.30 ± 0.05	53.18 ± 0.1	53.33 ± 0.06	53.01 ± 0.07	53.57 ± 0.09
MAP-TV	53.24 ± 0.05	53.31 ± 0.04	53.21 ± 0.09	53.40 ± 0.07	53.79 ± 0.17	53.67 ± 0.09
b						
MLEM	2.02 ± 0.07	1.63 ± 0.05	2.08 ± 0.06	1.42 ± 0.05	2.73 ± 0.12	1.73 ± 0.07
MAP-MRP	1.13 ± 0.04	1.04 ± 0.04	1.14 ± 0.08	1.15 ± 0.05	1.13 ± 0.07	1.27 ± 0.08
MAP-TV	1.03 ± 0.04	1.02 ± 0.04	1.24 ± 0.08	1.20 ± 0.06	1.81 ± 0.14	1.38 ± 0.08

improve the CoV or the bias of MLEM for the partial rings, but the standard deviation was lower with better TOF.

For the evaluation of the accuracy of reconstructed edges, sigmoid functions were fitted to averaged line profiles from the central slice and its two closest neighbors (along the red line in Fig. 2). The line profile was not calculated along the proton beam directions (which one needs to do to verify the proton range) because the edge in the PET image shows the edge of the lung in cases where the proton beam is stopped beyond this edge, and not the proton range. The sigmoid fit parameters for the MAP reconstructions are similar, with MRP being slightly better for partial ring configurations. TOF is effective in making the slopes of MLEM fits steeper (smaller b), but its effect on MAP results were minimal.

V. DISCUSSION

In this paper, MAP-MRP successfully improved the edge detection and image uniformity via the use of MRP for penalization in MAP reconstruction. The proposed penalty function was robust against the change in partial ring scanner configurations with low count statistics. The observations based on our results are in line with the results from Cabello *et al.* [13], which used the TV prior information for MAP-EM on pencil beam data for hadron therapy. In general, both MAP methods are robust against missing information due to the partial ring scanner configuration. MLEM, on the other hand, cannot compensate for the large gaps in the angular coverage without any regularization or very good TOF information.

The results from [13] indicate that if the MAP penalization parameter for TV is not selected carefully, the algorithm may not lead to a stable solution. This finding was also noted in the work of Kinouchi *et al.*, in which they compared the performances of MLEM with MAP with TV prior on pencil beam [18]. In this paper, MAP-MRP was much less sensitive to the choice of the regularization parameter (see Figs. 3 and 5) than MAP-TV. This was due to the use of a median filter in MRP, which preserves the intensity changes between different structures, while smoothening the intensity changes within the filter window. Stability of MRP against noise makes it possible to have strong penalization without introducing additional artifacts in the reconstructed images. The CoV and bias values are similar for the MAP methods, but a difference between MAP and MLEM reconstructions is visible.

The voxel size of $4 \times 4 \times 4$ mm^3 was selected due to the high noise in the data. A smaller voxel size of $2 \times 2 \times 2$ mm^3

was tested, and the line profiles were found too noisy to determine a reliable edge. For higher statistics, as was the case in [16] with coincidence counts from 15 M to 150 M, smaller voxel sizes could be used. But such statistics are not realistic in the proton therapy application considered here.

Previous studies have shown that TOF information generally improves the contrast recovery, increases the convergence speed and is less sensitive to noise and inconsistent data corrections [13], [16], [38]. Both MAP methods prevented the elongation and suppressed the noise efficiently. Therefore, the improvement of TOF did not result in a significant improvement for the images reconstructed with MAP methods. About 400 ps CRT was deemed sufficient to obtain sharp edges with the penalized MAP reconstruction methods. On the other hand, TOF information around 200 ps or better is needed with MLEM to achieve similar results as MAP reconstructions.

The MAP methods used in this paper reliably reconstructed clearer edges than MLEM, separating the object from the background. They were also better at reconstructing the images in the presence of missing angles. In addition to the shared advantages of MAP methods, the MAP-MRP approach achieved a better overall image quality without compromising the details in the image compared to MAP-TV. No additional artifacts were introduced by MAP-MRP while this was not the case for MLEM (increased noise throughout iterations) and MAP-TV (checkerboard artifacts). The low statistics limited the performance of MAP-TV, whereas MLEM performance deteriorated with low statistics as well as partial ring configurations. MAP-MRP was also robust in terms of the selection of the penalization weight, making it easy-to-use in clinics. Based on these observations, MRP within MAP method makes a suitable candidate for penalization for the reconstruction of in-beam PET data.

ACKNOWLEDGMENT

The authors would like to thank the Center for Information Technology of the University of Groningen for their support and for providing access to the Peregrine high-performance computing cluster.

REFERENCES

[1] M. T. Studenski and Y. Xiao, "Proton therapy dosimetry using positron emission tomography," *World J. Radiol.*, vol. 2, no. 4, pp. 135–142, 2010.

[2] C. H. Min *et al.*, "Clinical application of in-room positron emission tomography for in vivo treatment monitoring in proton radiation therapy," *Int. J. Radiat. Oncol. Biol. Phys.*, vol. 86, no. 1, pp. 183–189, May 2013.

[3] K. Parodi, "Vision 20/20: Positron emission tomography in radiation therapy planning, delivery, and monitoring," *Med. Phys.*, vol. 42, no. 12, pp. 7153–7168, Dec. 2015.

[4] T. Nishio *et al.*, "The development and clinical use of a beam ON-LINE PET system mounted on a rotating gantry port in proton therapy," *Int. J. Radiat. Oncol. Biol. Phys.*, vol. 76, no. 1, pp. 277–286, Jan. 2010.

[5] S. P. Nischwitz *et al.*, "Clinical implementation and range evaluation of *in vivo* PET dosimetry for particle irradiation in patients with primary glioma," *Radiotherapy Oncol.*, vol. 115, no. 2, pp. 179–185, May 2015.

[6] P. Dendooven *et al.*, "Short-lived positron emitters in beam-on PET imaging during proton therapy," *Phys. Med. Biol.*, vol. 60, no. 23, pp. 8923–8947, Dec. 2015.

[7] H. J. T. Buitenhuis, F. Diblen, K. W. Brzezinski, S. Brandenburg, and P. Dendooven, "Beam-on imaging of short-lived positron emitters during proton therapy," *Phys. Med. Biol.*, vol. 62, no. 12, pp. 4654–4672, Jun. 2017.

[8] A. Miyatake *et al.*, "Measurement and verification of positron emitter nuclei generated at each treatment site by target nuclear fragment reactions in proton therapy," *Med. Phys.*, vol. 37, no. 8, pp. 4445–4455, Jul. 2010.

[9] S. Surti and J. S. Karp, "Design considerations for a limited angle, dedicated breast, TOF PET scanner," *Phys. Med. Biol.*, vol. 53, no. 11, pp. 2911–2921, Jun. 2008.

[10] W. Enghardt *et al.*, "Charged hadron tumour therapy monitoring by means of PET," *Nucl. Instrum. Methods Phys. Res. Section A Accelerators Spectrometers Detectors Assoc. Equip.*, vol. 525, nos. 1–2, pp. 284–288, 2004.

[11] H. Tashima *et al.*, "Development of a small single-ring OpenPET prototype with a novel transformable architecture," *Phys. Med. Biol.*, vol. 61, no. 4, pp. 1795–1809, Feb. 2016.

[12] P. Crespo, G. Shakirin, and W. Enghardt, "On the detector arrangement for in-beam PET for hadron therapy monitoring," *Phys. Med. Biol.*, vol. 51, no. 9, pp. 2143–2163, May 2006.

[13] J. Cabello, I. Torres-Espallardo, J. E. Gillam, and M. Rafecas, "PET reconstruction from truncated projections using total-variation regularization for hadron therapy monitoring," *IEEE Trans. Nucl. Sci.*, vol. 60, no. 5, pp. 3364–3372, Oct. 2013.

[14] P. Crespo, G. Shakirin, F. Fiedler, W. Enghardt, and A. Wagner, "Direct time-of-flight for quantitative, real-time in-beam PET: A concept and feasibility study," *Phys. Med. Biol.*, vol. 52, no. 23, pp. 6795–6811, Dec. 2007.

[15] C. Kurz *et al.*, "Investigating the limits of PET/CT imaging at very low true count rates and high random fractions in ion-beam therapy monitoring," *Med. Phys.*, vol. 42, no. 7, pp. 3979–3991, Jun. 2015.

[16] S. Surti, W. Zou, M. E. Daube-Witherspoon, J. McDonough, and J. S. Karp, "Design study of an *in situ* PET scanner for use in proton beam therapy," *Phys. Med. Biol.*, vol. 56, no. 9, pp. 2667–2685, 2011.

[17] V. Y. Panin, G. L. Zeng, and G. T. Gullberg, "Total variation regulated EM algorithm," *IEEE Trans. Nucl. Sci.*, vol. 46, no. 6, pp. 2202–2210, Dec. 1999.

[18] S. Kinouchi *et al.*, "Total variation minimization for in-beam PET image reconstruction," in *Proc. IEEE Nucl. Sci. Symp. Conf. Rec.*, Anaheim, CA, USA, 2012, pp. 3412–3414.

[19] C. Hui, D. Robertson, and S. Beddar, "3-D reconstruction of scintillation light emission from proton pencil beams using limited viewing angles—A simulation study," *Phys. Med. Biol.*, vol. 59, no. 16, pp. 4477–4492, Aug. 2014.

[20] S. Alenius and U. Ruotsalainen, "Bayesian image reconstruction for emission tomography based on median root prior," *Eur. J. Nucl. Med.*, vol. 24, no. 3, pp. 258–265, Mar. 1997.

[21] S. Alenius, U. Ruotsalainen, and J. Astola, "Using local median as the location of the prior distribution in iterative emission tomography image reconstruction," *IEEE Trans. Nucl. Sci.*, vol. 45, no. 6, pp. 3097–3104, Dec. 1998.

[22] A. Seret, "Median root prior and ordered subsets in Bayesian image reconstruction of single-photon emission tomography," *Eur. J. Nucl. Med.*, vol. 25, no. 3, pp. 215–219, Mar. 1998.

[23] G. Kontaxakis *et al.* "Iterative image reconstruction for clinical PET using ordered subsets, median root prior, and a Web-based interface," *Mol. Imag. Biol.*, vol. 4, no. 3, pp. 219–231, Jun. 2002.

[24] U. Tuna, A. Sohlberg, and U. Ruotsalainen, "Can we reduce SPECT acquisition time using MAP-EM reconstruction?" *J. Pattern Recognit. Intell. Syst.*, vol. 1, no. 3, pp. 54–63, 2013.

[25] D. J. Kadrmas, "LOR-OSEM: Statistical PET reconstruction from raw line-of-response histograms," *Phys. Med. Biol.*, vol. 49, no. 20, pp. 4731–4744, Oct. 2004.

[26] A. J. Reader, "List-mode EM algorithms for limited precision high-resolution PET image reconstruction," *Int. J. Imag. Syst. Technol.*, vol. 14, no. 3, pp. 139–145, 2004.

[27] A. J. Reader, K. Erlandsson, M. A. Flower, and R. J. Ott, "Fast accurate iterative reconstruction for low-statistics positron volume imaging," *Phys. Med. Biol.*, vol. 43, no. 4, pp. 835–846, 1998.

[28] C. Katoh *et al.*, "Iterative reconstruction based on median root prior in quantification of myocardial blood flow and oxygen metabolism," *J. Nucl. Med.*, vol. 40, no. 5, pp. 862–867, 1999.

[29] S. Alenius and U. Ruotsalainen, "Generalization of median root prior reconstruction," *IEEE Trans. Med. Imag.*, vol. 21, no. 11, pp. 1413–1420, Nov. 2002.

[30] J. Allison, "Facilities and methods: Geant4—A simulation toolkit," *Nucl. Phys. News*, vol. 17, no. 2, pp. 20–24, Aug. 2007.
[31] S. Jan *et al.*, "GATE V6: A major enhancement of the GATE simulation platform enabling modelling of CT and radiotherapy," *Phys. Med. Biol.*, vol. 56, no. 4, pp. 881–901, Feb. 2011.
[32] R. L. Siddon, "Fast calculation of the exact radiological path for a three-dimensional CT array," *Med. Phys.*, vol. 12, no. 2. pp. 252–255, 1985.
[33] H. T. Van Dam, G. Borghi, S. Seifert, and D. R. Schaart, "Sub-200 ps CRT in monolithic scintillator PET detectors using digital SiPM arrays and maximum likelihood interaction time estimation," *Phys. Med. Biol.*, vol. 58, no. 10, pp. 3243–3257, May 2013.
[34] (2014). *Philips Vereos PET/CT*. Accessed: Mar. 30, 2017. [Online]. Available: http://incenter.medical.philips.com/doclib/enc/10264938/452296298357_VereosBrochureREV_FNL_HR.pdf?func=doc.Fetch&nodeid=10264938&vernum=1
[35] S. Helmbrecht *et al.*, "Analysis of metabolic washout of positron emitters produced during carbon ion head and neck radiotherapy," *Med. Phys.*, vol. 40, no. 9, Sep. 2013, Art. no. 091918.
[36] C. Burger *et al.*, "PET attenuation coefficients from CT images: Experimental evaluation of the transformation of CT into PET 511-keV attenuation coefficients," *Eur. J. Nucl. Med.*, vol. 29, no. 7, pp. 922–927, 2002.
[37] C. Robert *et al.*, "PET-based dose delivery verification in proton therapy: A GATE based simulation study of five PET system designs in clinical conditions," *Phys. Med. Biol.*, vol. 58, no. 19, pp. 6867–6885, 2013.
[38] M. Conti, "Focus on time-of-flight PET: The benefits of improved time resolution," *Eur. J. Nucl. Med. Mol. Imag.*, vol. 38, no. 6, pp. 1147–1157, Jun. 2011.